Measuring surface wave phase velocities beneath small broad-band arrays: tests of an improved algorithm and application to the French Alps.

Helle A. Pedersen, Olivier Coutant, Anne Deschamps, Michel Soulage, Nathalie Cotte

Geophys. J. Int. (2003) **154,** 903–912

Measuring surface wave phase velocities beneath small broad-band arrays: tests of an improved algorithm and application to the French Alps

Helle A. Pedersen,[1] Olivier Coutant,[1] A. Deschamps,[2] M. Soulage[1] and N. Cotte[1]

[1]*Laboratoire de Géophysique Interne et Tectonophysique, Observatoire de Grenoble,* BP 53x, F-38041 *Grenoble Cedex, France. E-mail: Helle.Pedersen@obs.ujf-grenoble.fr*

[2]*CNRS, Sophia Antipolis* 250, *Rue Albert Einstein,* 06560 *Valbonne, France*

Accepted 2003 April 11. Received 2002 December 9; in original form 2002 May 13

SUMMARY

The local measurement of dispersion curves of intermediate-period surface waves is particularly difficult because of the long wavelengths involved. We suggest an improved procedure for measuring dispersion curves using small-aperture broad-band arrays. The method is based on the hypotheses of plane incoming waves and that averaging over a set of events with a good backazimuth distribution will suppress the effects of diffraction outside the array. None of the elements of the processing are new in themselves, but each step is optimized so we can obtain a reliable dispersion curve with a well-defined uncertainty. The method is based on the inversion for the slowness vector at each event and frequency using time delays between pairs of stations, where the time delays Δt are obtained by frequency-domain Wiener filtering. The interstation distance projected on to the slowness vector (D) is then calculated. The final dispersion curve is found by, at each frequency, calculating the inverse of the slope of the best-fitting line of all (D, Δt) points. To test the algorithm, it is applied to synthetic seismograms of fundamental mode Rayleigh waves in different configurations: (1) the sum of several incident waves; (2) an array located next to or above a crustal thickening; and (3) added white noise, using regular and irregular backazimuth distributions. In each case, a circular array of 23 km diameter and composed of six stations is used. The algorithm is stable over a large range of wavelengths (between half and a tenth of the array size), depending on the configuration. The situations of several, simultaneously incoming waves or neighbouring heterogeneities are well handled and the inferred dispersion curve corresponds to that of the underlying medium. Above a strong lateral heterogeneity, the inferred dispersion curve corresponds to that of the underlying medium up to wavelengths of eight times the array size in the configuration considered, but further work is needed to better understand the limits under which the obtained dispersion curve is not biased. In the case of 5 per cent spectral amplitude white noise, the dispersion curve is also stable for wavelengths up to approximately eight times the array size, but this limit depends of course strongly on the noise level. The method is finally applied to data from two arrays in the French Alps located 50 km apart. It is possible to measure the dispersion curves up to wavelengths approximately ten times bigger than the array diameter. The difference in the dispersion curves is compatible with a crustal and lithospheric thickening under the Alps. However, the observed errors are large, which result in severe limits on the interpretation in terms of lithospheric structure. Longer recording periods may help to reduce the errors. Otherwise the algorithm is likely to be of use mainly in areas where the lateral variations outside the array are smaller than those of the French Alps.

Key words: array, broad-band, lithosphere, surface waves.

1 INTRODUCTION

Intermediate-period (10–100 s) teleseismic surface waves have the potential of resolving lateral heterogeneities of the lithosphere. However, some of the changes in the lithosphere are very abrupt. Examples are Moho steps or other abrupt Moho topography and dipping slabs, which may produce significant diffractions. Classical two-station methods can therefore be difficult to carry out,

especially at long periods when the distance between stations is of the order of the wavelength or smaller. Several regional methods are available, which use a 2-D array of stations, such as those based on ray theory (Yanovskaya 1996; Bruneton *et al.* 2002) or on the acoustic wave equation (Friederich & Wielandt 1995; Friederich 1998). However, these methods have at best a lateral resolution of the order of 100–200 km and require a large number of broad-band sensors.

Various techniques are available for estimating the slowness vector across an array (e.g. Capon 1969; Schmidt 1986; Goldstein & Archuleta 1987; Frankel *et al.* 1991; Mori *et al.* 1994; Bear & Pavlis 1997), using for example cross-correlation techniques, frequency–wavenumber analysis and different filtering and wave separation methods.

The calculation of local long-period dispersion curves is somewhat different from the majority of array processing techniques in that the aim is to stabilize the phase velocity estimation across an array with a diameter that is a fraction of the longest wavelength rather than to deduce information from each individual event. This is far from trivial due to the presence of coherent and incoherent noise. Classically it is considered that the closer the stations are, the more difficult it is to measure the phase velocities. However, shrinking the array to a fraction of a wavelength has the advantage of ensuring that the waves that are measured on different stations are almost the same, except for a small frequency-dependent delay. So even though the same amount of noise has stronger effects on the phase velocities measured at closely located stations compared with distant ones, the waves are much more coherent.

Another, more fundamental, problem is to establish the relationship between the observed dispersion curve and the structure beneath an array which is of the order of half to a tenth of the wavelength. In the case of a laterally homogeneous structure the array measurements can be used directly to invert for the local shear wave velocity with depth, something which is of use in stable oceanic or continental areas or on a smaller scale for example for shallow seismic investigations. In the case of laterally heterogeneous areas, it still remains to be shown what the exact conditions are under which the observed dispersion curve corresponds to that of the local structure. Even though we here mainly focus on the signal processing aspects in different noise configurations, the analysis of synthetic seismograms and field data from arrays located on laterally heterogeneous structures give some indication that it may be feasible to use array measurements to characterize lateral variations of the lithosphere.

Cotte *et al.* (2000) suggested a method for calculating dispersion curves where the time delays were calculated by the doublet method (Poupinet *et al.* 1984) in three frequency bands and using a sliding time window. The estimated backazimuths were then used to calculate interstation distances projected on to the slowness vector, and the phase velocity was obtained by linear regression using the (distance, delay) couples from all events. Cotte *et al.* (2002) applied this method to data from northern Europe, where the proposed lithospheric structure corresponds well to independently obtained results from teleseismic *P*-wave tomography (Arlitt 1999; Shomali *et al.* 2002) and lithospheric thicknesses obtained by anisotropy estimations (Plomerovà *et al.* 2002) The main drawback of the method used by Cotte *et al.* (2000) is that the backazimuth is measured in only three frequency bands, making it difficult to accurately estimate the backazimuth at each frequency. The measurement of the backazimuth in any of the three frequency intervals is difficult (and typically they have to be picked by hand) as the backazimuth varies with time within the filtered signal.

Here we suggest a more efficient procedure for measuring dispersion curves using a small broad-band array. We combine Wiener filtering with an inversion for the slowness vector using the L1 norm, and combine information from all available events to obtain the phase velocities beneath the array. No visual inspection of individual events is necessary, except for the individual frequency–time filtering of the signals.

The hypothesis behind the algorithm is that diffraction effects outside the array are averaged out with a well-distributed set of events, as this compensates for the difference between the structural and dynamic velocities that were pointed out by Wielandt (1993). We also make an assumption common in this type of analysis: that the wave fronts are close to a plane, due to the array diameters being between half and a 15th of a wavelength. During the processing we eliminate events at frequencies where the data cannot be well fitted to a plane wave.

We carry out a series of tests on synthetic seismograms to assess how our algorithm accommodates different types of noise. We separate the noise into three cases: (1) coherent noise in the form of plane Rayleigh waves incident from other backazimuths than that of the main incident wave; (2) noise generated by an underlying or neighbouring heterogeneous structure; (3) random noise.

Finally, we measure dispersion curves using two small arrays in the French Alps. The data constitute a good test of the stability of the algorithm under difficult conditions as we use data from fairly short field experiments (6 months and 1 yr), with rather simple installations of broad-band sensors and located in a strongly heterogeneous area.

2 METHOD

Prior to the array analysis of field data we correct for the instrument responses and filter the signals in the frequency–time domain using a phase-match filter (Herrin & Goforth 1977; Levshin *et al.* 1989). This filtering must be done very carefully, however, the same filter can be applied to all stations for each event as the stations are located very closely together compared with the distance between the source and the receiver.

The algorithm behind the array analysis is simple. It is summarized here, followed by a short discussion of each of its constituents. $\Delta t_{ij}^{k}(f)$ is the measured delay time between stations i and j at frequency f and for event k, and $D_{ij}^{k}(f)$ is the distance between stations i and j projected on to the best-fitting slowness vector at frequency f and for event k. $baz^{k}(f)$ is the backazimuth as a function of frequency for event k and $C(f)$ is the phase velocity.

For all events k:
  For all station couples (i, j):
    Calculate $\Delta t_{ij}^{k}(f)$ by Wiener filtering
  For all frequencies f:
    Calculate $baz^{k}(f)$ and $D_{ij}^{k}(f)$ by inversion of $\Delta t_{ij}^{k}(f)$ and using L1 norm
For all frequencies f:
  Calculate $C(f)$ by inversion of $(D_{ij}^{k}(f), \Delta t_{ij}^{k}(f))$ using L1 norm.

The first step of the analysis is to measure the time delay $\Delta t_{ij}^{k}(f)$ as a function of frequency f for each event and station couple (ij). We use Wiener filtering for this measurement (Wiener 1949; Hwang & Mitchell 1986), transforming phase differences ϕ to time delays using $dT = (\phi/2\pi f)$. Wiener filtering has the advantage of objectively smoothing the spectra and reducing incoherent noise. We smooth the spectra applying an nth-order Hanning window to

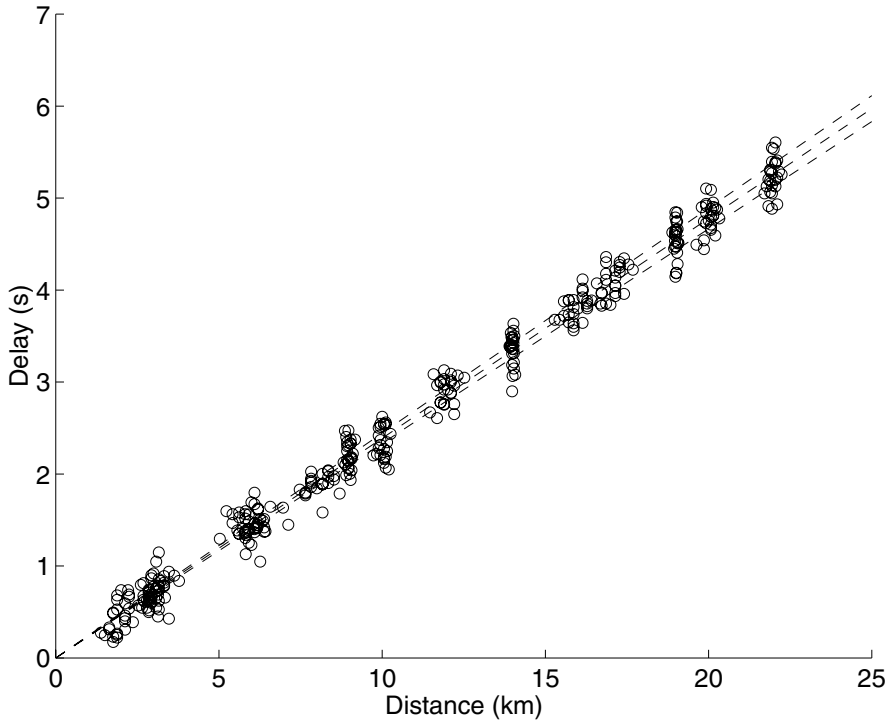

Figure 1. Example of calculation of the phase velocity and its uncertainty at one frequency (0.02 Hz) using synthetic seismograms in a flat-layered model with 5 per cent added noise (see Subsection 3.3 and Fig. 6). The circles show all the (distance-delay) points obtained through the backazimuth calculation for each event. The three dashed lines shown the straight lines that correspond to minimum, average and maximum slowness.

the cross-correlation of the two signals. We reject phases that were measured with a coherence of less than 0.99. The order n of the Hanning window may be somewhat variable, depending on the signal. We typically choose a low degree of smoothing (Hanning order of 2–8) for the phase estimation and a slightly higher value for the estimation of the coherence.

The second step is to invert the time delays $\Delta t_{ij}^k(f)$ for each event k to obtain the best slowness vector $\mathbf{p}_k$, and store distances $D_{ij}^k(f)$ between station pairs projected on to the slowness vector as well as the misfit $F^k(f)$. It is crucial to reduce the influence of outliers, so the misfit is estimated as the mean absolute difference (L1 norm) between the observed and estimated delays. A simple and robust procedure for doing this is to search for the backazimuth for which the corresponding $(D_{ij}^k(f), \Delta t_{ij}^k(f))$ points can best (in terms of low misfit) be described by a line that goes through the origin. In practice, the results are almost identical independently of whether it is the slowness or the velocity that is estimated. As the error associated with the station locations is much smaller than that associated with the time delay, the misfit should be calculated as the average difference in time between the observed delays and the best-fitting line.

The phase velocity dispersion curve for each event can be obtained as the inverse of the best-fitting line, estimated at each frequency. Even small amounts of noise strongly influence the phase velocities so the dispersion curve obtained from any individual event is unreliable. The unreliable phase velocities may also be due to us measuring the dynamic rather than the structural velocity (Wielandt 1993). The phase velocity is therefore finally calculated at each frequency using all observed $(D_{ij}^k(f), \Delta t_{ij}^k(f))$ points that are associated with a misfit lower than a certain threshold. A threshold is necessary as a high misfit indicates that a plane wave is not a good solution to the inversion from which the point was obtained, either due to noise or diffraction effects. The velocity V is calculated as the inverse of the slope of the best-fitting line $\Delta t = D/V$, where D is the distance, again using the L1 norm (see Fig. 1). The procedure is repeated for all frequencies and corresponds to averaging the phase velocities associated with each event and weighted by the number of station couples used for the event.

The estimation of the uncertainty is somewhat difficult. The main problem is the rejection of points that correspond to a high misfit, so that a normal bootstrap procedure would be somewhat obscure, because only a subset of the events is used for each frequency. We therefore use the mean absolute misfit $F(f)$ taking into account that the straight line must go through the origin, by calculating the upper and lower limits for V as

$$V_{\min}(f) = \frac{D_{\max}(f)}{[D_{\max}(f)/V(f) + F(f)]}$$
$$V_{\max}(f) = \frac{D_{\max}(f)}{[D_{\max}(f)/V(f) - F(f)]}, \quad (1)$$

where $D_{\max}$ is the maximum value of $D_{ij}^k(f)$. This corresponds to calculating the slope of the straight line if the misfit was added (or subtracted) to the time measured at the furthest distance (see Fig. 1). The corresponding uncertainty is approximately twice that obtained by a bootstrap procedure, but it corresponds fairly closely to the standard deviation in the case where the number of stations available is the same for all events.

3 TESTS ON SYNTHETIC SEISMOGRAMS

The array measurements can potentially be perturbed by both coherent and incoherent noise. The coherent noise can have an origin in simultaneous incoming waves (which may form a curved or

undulating wave front), or in closely located lateral heterogeneities. In this section we independently test the stability of the algorithm in these different cases. For simplicity, we use the same basic crustal model for all the simulations: a 40 km thick layer over a half-space. The wave velocities are 6.7 km s^{-1} in the layer and 8.2 km s^{-1} in the half-space. $V_p/V_s = 1.73$ in both the layer and the half-space. The densities are 2.7 and 3.2 g cm^{-3}, respectively. Throughout the numerical tests, we use records from six stations located in a circular array of 23 km diameter.

3.1 Sum of plane incoming waves

Wielandt (1993) has shown the difficulty of extracting the structural velocity at a constant frequency if more than one plane wave is incident. To test the algorithm in this situation we calculated the fundamental mode Rayleigh wave in the plane-layered reference model, and then added three randomly chosen fundamental mode Rayleigh waves incident from other directions (between $\pm 90^\circ$ of the direction of the main wave). The spectral amplitude of each of these three waves was chosen randomly between 0 and 20 per cent of the spectral amplitude of the main wave. A limit of 20 per cent is very generous, as secondary plane waves are unlikely to be created with an amplitude higher than 5–10 per cent (see, for example, Pedersen *et al.* 1998). Fig. 2 shows the calculated phase velocities when the algorithm has been applied using five, ten or 15 different events. It shows that the problem with several interfering plane waves is reliably handled by the algorithm that we propose. This result may seem surprising considering the big differences between structural and dynamic phase velocities (pointed out by Wielandt 1993) for an incoming Rayleigh wave 'polluted' by a very small-amplitude Rayleigh wave incident from another direction. The measurement is stable because of the Wiener filtering, as it effectively smooths out oscillations produced by interference of the different incoming waves. In the case of a single additional wave, the oscillations were stronger than when three additional waves were considered. In this case, spectral amplitudes of the additional wave of 5–10 per cent were well handled if more than five 'events' were used.

3.2 Coherent noise due to a laterally heterogeneous structure

Synthetic seismograms were calculated using the 2.5-D indirect boundary element method (IBEM, for a detailed discussion see Sànchez-Sesma & Campillo 1993) adapted to plane surface waves obliquely incident upon a 2-D structure (Pedersen *et al.* 1996). The advantage of IBEM is that it calculates the full wavefield with all types of coupling between waves, thereby producing local diffractions of a realistic amplitude as compared with real data. We use a simple model of a homogeneous crust over a homogeneous half-space (see Fig. 3), with a crustal thickness increasing from 40 km on the edge to 55 km in the centre of the model, and elastic parameters as used in the previous section. Two arrays (A and B) are located at the surface at positions shown by triangles in Fig. 3. Array A is located 50 km outside the crustal thickening and array B is located at an arbitrarily chosen position above it.

For numerical reasons (see Pedersen *et al.* 1994), the numerical simulations are unstable for surface waves incident close to the strike of the model (here east and west). As the model is 2-D, the simulation results are equal (except for a different sign of the slowness along-strike) for waves incident symmetrically around the cross-section (for example, N010 and N350). Consequently, we only explored backazimuths between N000 and N070, and N180 and N250.

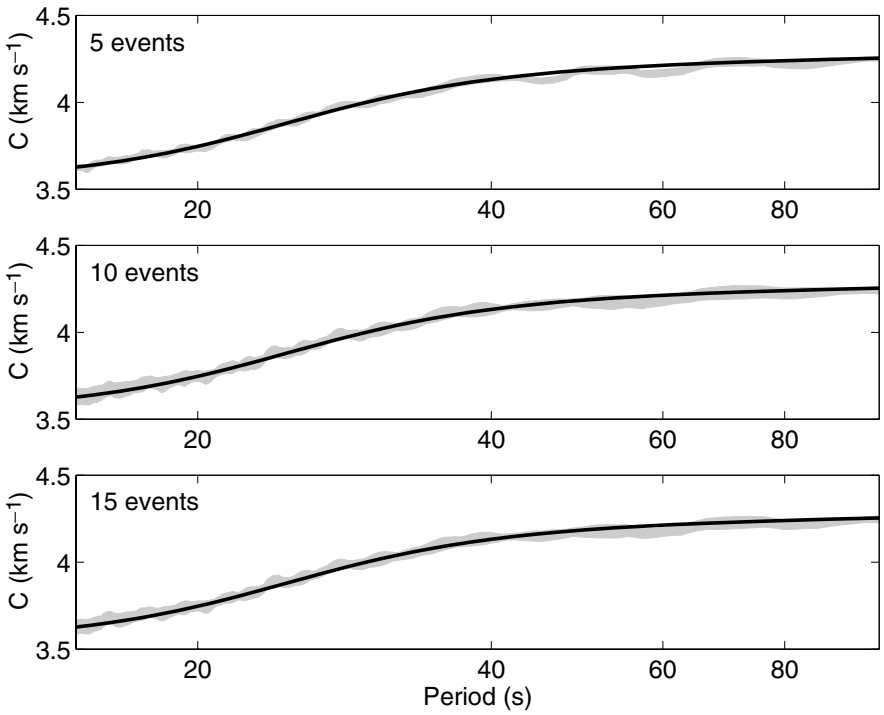

Figure 2. Phase velocities (grey-shaded areas) obtained by array analysis using a circular array and a sum of one main and three secondary plane incident waves. The secondary waves have random directions within $\pm 90^\circ$ of the main wave and a constant spectral ratio with the main wave chosen randomly between 0 and 0.2. The three figures correspond to different number of 'events' used in the analysis, varying from 5 (top) to 15 (bottom). The black line shows the theoretical dispersion curve for the input model.

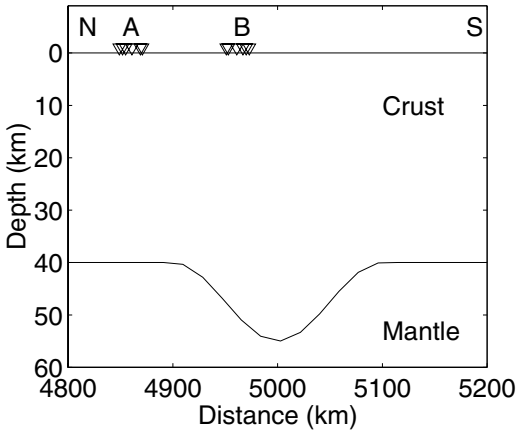

Figure 3. Laterally varying 2-D model used in the simulations. A one-layer crust ($V_p = 6.7$ km s^{-1}, $V_s = 3.84$ km s^{-1}, $\rho = 2.7$ g cm^{-3} is thickened from 40 km in the northern and southern parts of the model to 55 km in the centre of the model. The mantle is characterized by $V_p = 8.2$ km s^{-1}, $V_s = 4.74$ km s^{-1}, $\rho = 3.2$ g cm^{-3}. The locations of the two arrays (A and B) are shown by the location of the triangles at the surface.

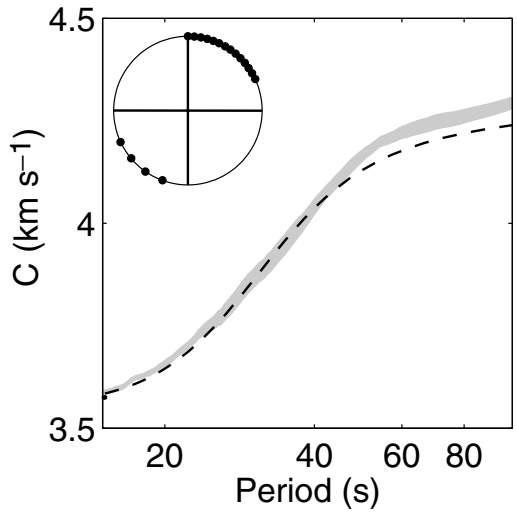

Figure 5. Phase velocities within their uncertainties (grey area) calculated for array B using an irregular backazimuth distribution (polar plot in top left corner). The dispersion curves of 40 and 55 km thick crustal models are shown by dotted lines and that of a 50.6 km thick crustal model (equal to the crustal thickness beneath array B) is shown by the dashed line.

Fig. 4 shows the dispersion curves within the uncertainty (grey area) obtained for array A with even and uneven backazimuth distributions (Figs 4a and b). For comparison, we included dispersion curves for a 40 and a 55 km thick crust (dashed and dotted lines). Even though the neighbouring structure introduces slight oscillations in the dispersion curve, due probably to wave diffraction effects, the dispersion curve has a very small uncertainty and corresponds to the medium below the array until a 100 s period, i.e. a wavelength of 420 km (i.e. a wavelength twice the width of the crustal thickening).

Only small changes occurred for array B between the dispersion curves for the even and uneven backazimuth distributions. Fig. 5 shows the dispersion curve for array B in the case of an uneven backazimuth distribution, as well as three reference dispersion curves corresponding to the thinnest and thickest crust (dotted lines) and a 50.3 km thick crust corresponding to the crustal thickness beneath the centre of the array (dashed line). The dispersion curve has a small uncertainty up to 100 s period, however, at approximately 50 s period (210 km wavelength) the dispersion curve deviates from the dashed line, showing that the dispersion curve is biased by diffraction effects. Array B exhibits a typical behaviour of the dispersion curves above the thickened crust, with the difference between observed and local dispersion curves somewhat model and location dependent. The period where the observed dispersion curve deviated from the target was typically located at 50–60 s period.

These results show that further theoretical developments need to be carried out to determine the limitations of the interpretation of dispersion curves measured in small arrays. However, these preliminary results are quite encouraging concerning the use of dispersion curves measured by small arrays and shows that the algorithm is also stable in complex geometries.

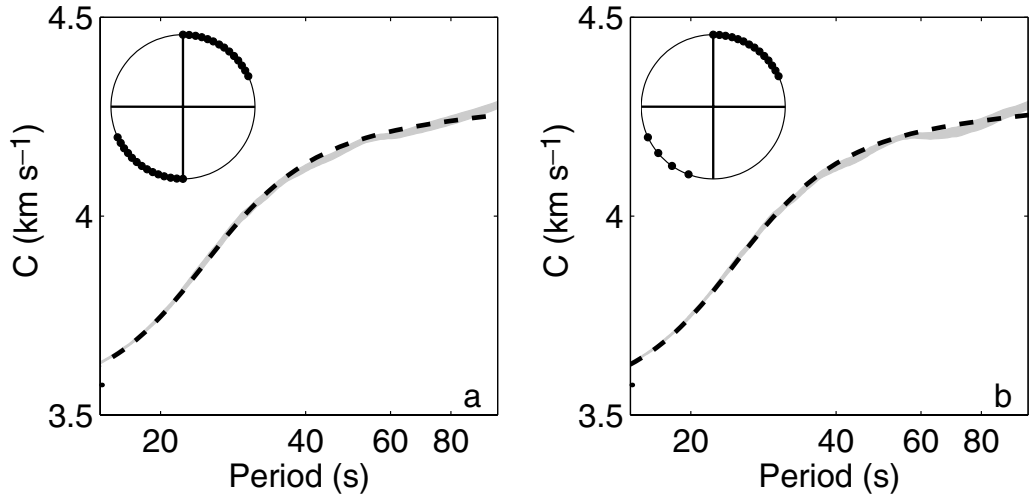

Figure 4. Phase velocities within their uncertainties (grey area) calculated for array A. The dispersion curve of the 40 km thick crustal model is shown by the dashed line and that of a 55 km thick crustal model is shown by the dotted line. Polar plot in the top left-hand corners show the backazimuths of the incident waves: (a) regular backazimuth distribution; (b) irregular backazimuth distribution.

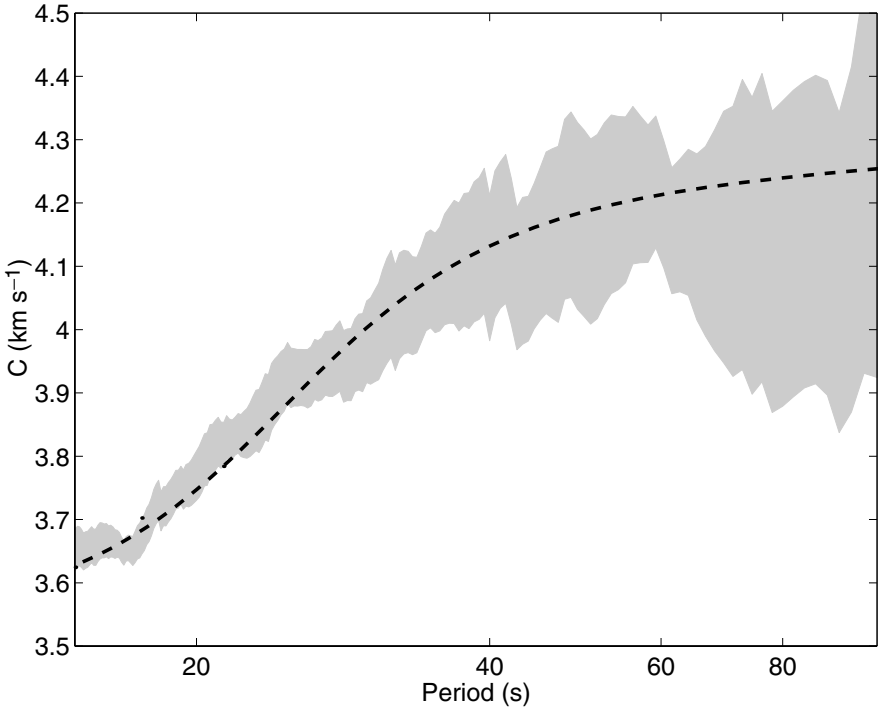

Figure 6. Phase velocities within their uncertainties (grey area) calculated using the flat-layered reference model (constant 40 km thick crust) and 5 per cent random noise added to the seismograms. The predicted dispersion curve is shown by the dashed line, and the average velocity of all individual measurements ± one standard deviation are shown by the dotted lines.

3.3 Random noise

The seismograms with a single incident wave in a laterally homogeneous model were then contaminated by random noise. We chose a noise level of 5 per cent, which is realistic and possibly even somewhat high compared with field data with a careful selection of teleseismic events followed by subsequent frequency–time filtering (see, for example, Levshin *et al.* 1989). Fig. 6 shows the dispersion curve using seven different realizations of noisy seismograms, i.e. seven 'events'. The random noise is clearly more difficult to handle than the coherent plane wave noise. Even though the velocities of the individual events are unreliable, the observed backazimuths are nevertheless generally measured within a 3°–5° uncertainty. In the case presented here the measurement is fairly stable up to a 60 s period, i.e. an order of magnitude larger than the diameter of the array, but this value is of course dependent on the noise level. Even though the random noise has a strong influence on the uncertainty of the measurement, it does not introduce systematic errors. In Fig. 6 we also show the average dispersion curve ± one standard deviation (dotted line).

4 DISPERSION CURVES MEASURED BY ARRAYS IN THE FRENCH ALPS

The French Alps are characterized by very strong lateral heterogeneities with significant surface and Moho topography (see Fig. 7 and, for example, Thouvenot *et al.* 2002). To illustrate the difficulty of calculating phase velocities in the area with a two-station method we show the result of such an analysis using data from permanent broad-band stations in the area (circles in Fig. 7).

Events were selected with a great-circle path at an angle of less than 2° to the great circle between the stations. Depending on the station pair, 2–3 years of recording were available, but we used only the few events where the phase velocity was measured with more than 0.99 coherence. We time–frequency filtered the vertical component to enhance the fundamental mode Rayleigh wave and calculated dispersion curves using Wiener filtering (Wiener 1949; Hwang & Mitchell 1986). In Fig. 8 we show an example of this analysis for two paths, SSB-NICE and SSB-OGGM. The SSB-NICE path corresponds to all the measurements between SSB and one of the three permanent broad-band stations close to Nice, on average located 250 km from SSB. SSB and OGGM are located 123 km apart. There are clearly severe problems in the measurements, and surprisingly the dispersion curves of SSB-NICE are as unstable as the SSB-OGGM ones, even though we would expect the error to decrease with increasing distance. This may be because the waves propagate on a very oblique path compared with the Alpine arc.

Fig. 7 also shows the station location of the two temporary broad-band arrays that we used in the analysis (STS2 and CMG3-ESP 90 s sensors). The first array (five temporary stations, shown as triangles) had a diameter of 23 km and was located in the Briançon area for a duration of 6 months. The second array (four stations, shown as squares) had a diameter of 45 km and was located close to Grenoble, in the external crystalline massif of Belledonne, for a duration of 15 months. Recording conditions were generally good as the sensors were installed on very shallow sedimentary fillings or directly on bedrock. In each case one permanent station of the ROSALP broad-band array was part of the array. The centres of the arrays were located 50 km apart.

The measured dispersion curves for the Briançon and Grenoble arrays are shown in Fig. 9. 24 events were used in the analysis of the Briançon array and 54 for the Grenoble array. The events were well distributed in both epicentral distance and backazimuth, as shown on the inlets. After rejection of points with a bad fit, the number of

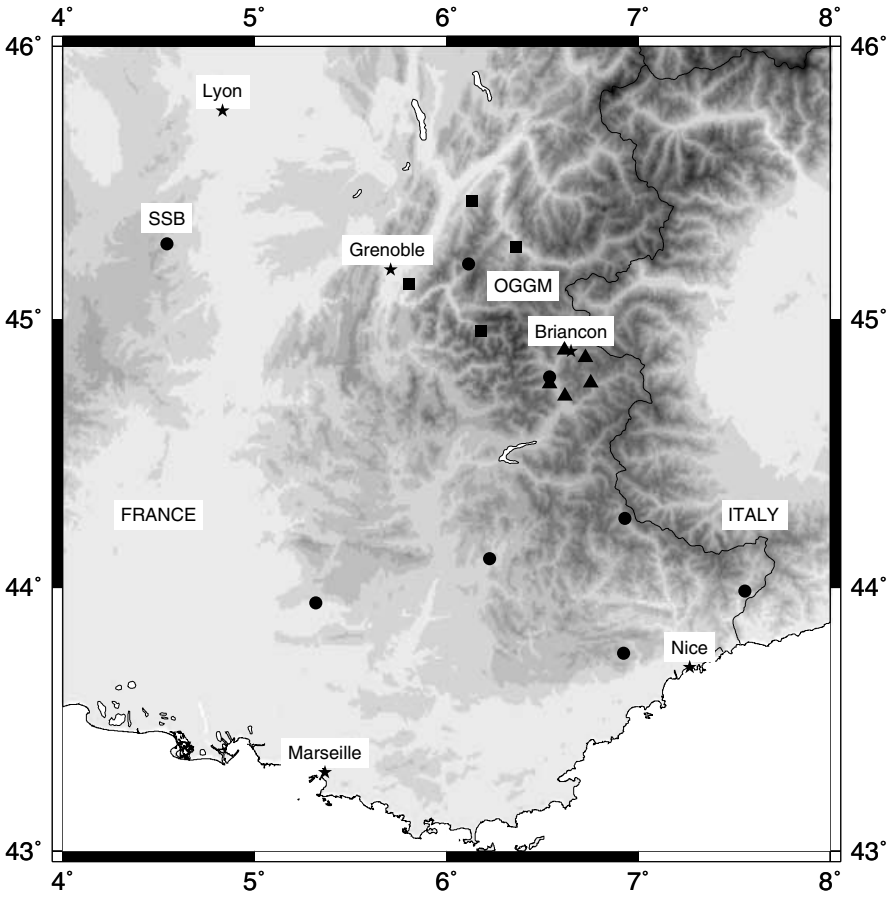

Figure 7. Topographic map of the French Alps. The two arrays are shown with squares (Grenoble array) and triangles (Briançon array). Permanent stations are shown with circles. Note that OGGM is the permanent station in the centre of the Grenoble array. Grenoble, Briançon and major cities are also shown (stars).

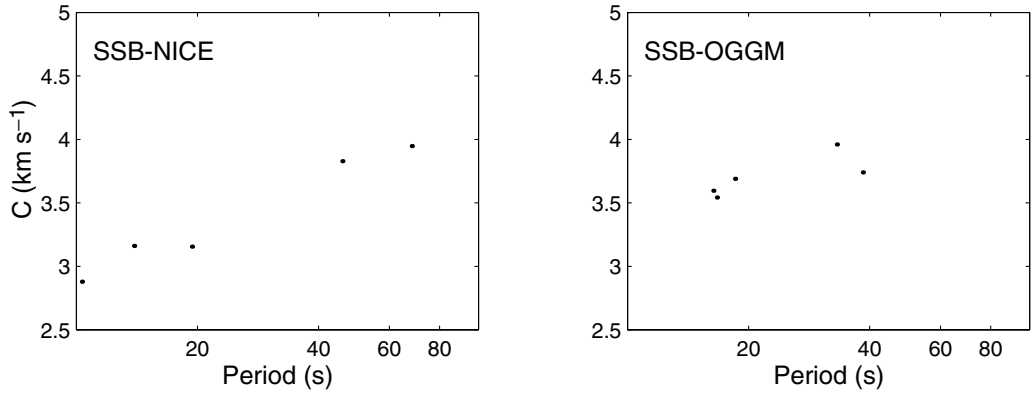

Figure 8. Example of two-station phase velocity measurements using permanent broad-band stations. SSB and OGGM are located 123 km apart while SSB is located approximately 250 km from the three stations near Nice.

events used for the Briançon array at each frequency varied from 8 to 14 at periods up to 50 s, and from four to six at 50–70 s period. For the Grenoble array, 23–40 events were used at each frequency out of the total of 54 events. Removing random sets of 27 events did not change the dispersion curve for the Grenoble array apart from making it less smooth and increasing the estimated error. Note that the error bars are slightly smaller than those obtained in the two-station analysis (Fig. 8). This result is rather encouraging considering that the diameter of the Grenoble array is 2.7 and 5.5 times smaller than the length of the two profiles. However, the error bars are still too high to provide very strong constraints on the lithospheric structure. It is interesting that the uncertainty does not evolve very much with period. This may be explained by the trade-off between two causes: strong Moho variation near the array mostly deteriorate the short-period part of the dispersion curve, but random noise has the most negative effect at long periods where small phase errors have

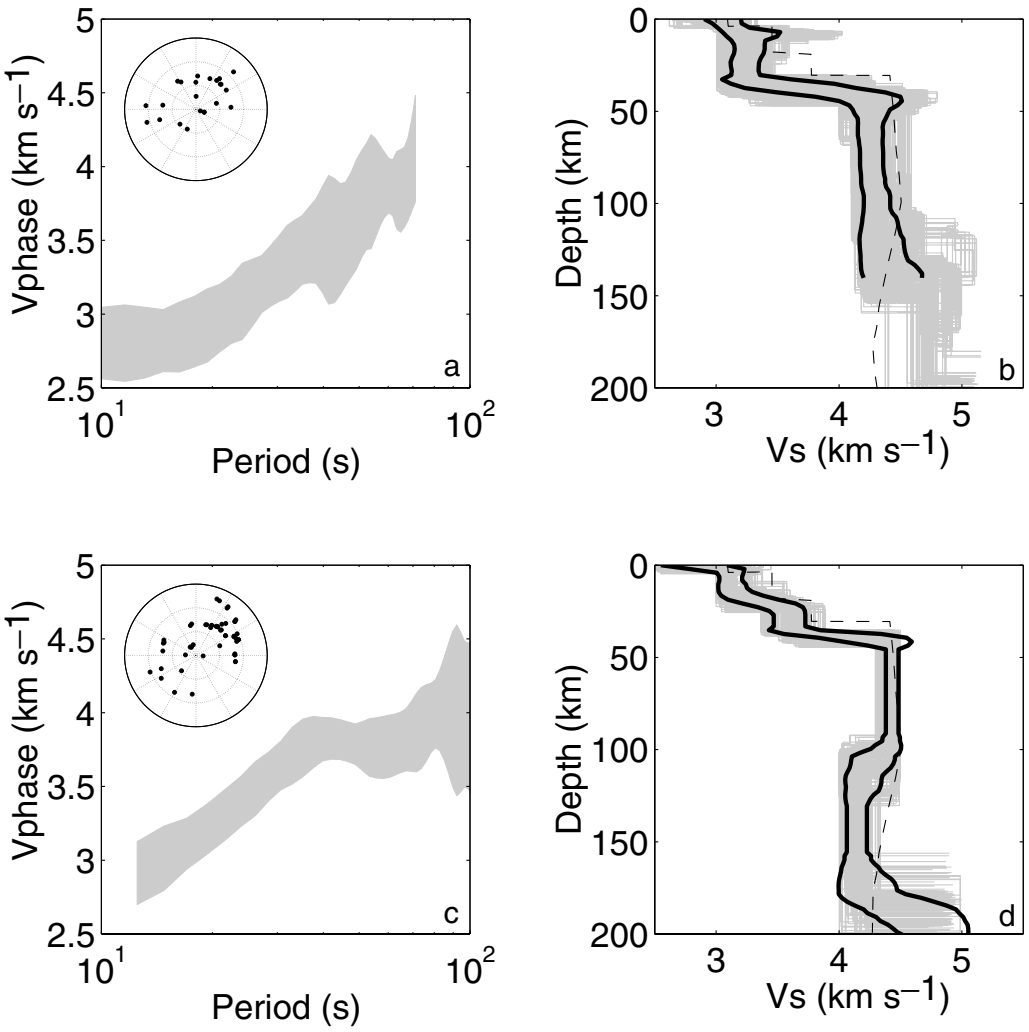

Figure 9. Dispersion curves for the Briançon (a) and Grenoble (c) arrays. The grey area indicates the uncertainty of the measurements. The event distribution in polar plots centred on the arrays are shown as inlets. The result of the inversion are shown to the right for the two arrays (b, Briançon; d, Grenoble). The acceptable models are shown with grey lines. The bold black lines show the average of the acceptable models ± one standard deviation. Note that the Briançon models are resolved to a maximum of 140 km. The average model of beneath Western Europe (Dost 1990) is shown by the dashed line.

a strong influence on the velocities. Considering the error bars, fine changes in mantle structure cannot be resolved by the method, while it may still be possible to identify major changes.

We used a Monte Carlo-type inversion as presented by Shapiro *et al.* (1997) to invert for the Earth structure. The inversions (Figs 9b and d) show all acceptable Earth models (thin grey lines) and the average dispersion curve ± one standard deviation. The shear wave velocities were constrained to 4.0–5.0 km s^{-1} in the uppermost mantle and 4.0–5.5 km s^{-1} in the deepest mantle layers so as to avoid very unrealistic models. The models show that the observed dispersion curves are coherent with the known crustal structure of the area and with the hypothesized upper-mantle structure. Beneath the Grenoble array, the models show a crustal thickness of approximately 40 km and a total lithospheric thickness of approximately 100 km, which corresponds to the average value for Western Europe (Dost 1990, dashed line). Beneath the Briançon array, the models show a crustal thickness is approximately 50 km and a total lithospheric thickness of at least 140 km, beneath which the resolution is very poor due to the limited frequency range of the dispersion curve. The average model shows rather low V_s compared with the curve suggested by Dost (1990), but a significant subset of the models have higher velocities. The variability of the models show that the high uncertainties on the dispersion curve induce a limited resolution on the mantle structure. However, none of the acceptable models have a low-velocity layer in the upper 140 km. This apparent thickening is compatible with either a lithospheric subduction or thickening beneath the Alps, as suggested by global tomography models (Spakman 1990), local teleseismic tomography (Guyoton 1991) or earthquake locations (Cattaneo *et al.* 1999). The interpretation of this dispersion curve may be biased by systematic errors due to the laterally heterogeneous structure beneath the Briançon array. This type of bias is likely to be smaller than for the two-station measurements where it was possible to use only a very few events and two propagation directions.

5 CONCLUSIONS

Dispersion curves of intermediate-period (10–100 s) surface waves are particularly difficult to measure on a regional scale due to their

long wavelength. Array measurements offer an attractive alternative, especially as the interpretation of dispersion curves is potentially simpler than with a tomographic approach.

None of the techniques used in the array measurement presented here are new. However, we succeeded in obtaining a robust procedure through the use of frequency–time filtering prior to the analysis, Wiener filtering and the L1 norm in the inversions. The algorithm is sufficiently stable to be semi-automatic in the sense that the array processing is automatic. The preprocessing should be done very carefully, and requires manual intervention to obtain the best possible frequency–time filtering.

It is not quite clear exactly which area is characterized by the resulting dispersion curve. Full waveform 3-D synthetics using a method with no inherent approximations needs to be performed to answer this question. However, it is encouraging that for the 2-D crustal thickening considered here the observed dispersion curve corresponds to the local dispersion curve even with very close heterogeneities, and that above the crustal thickening a similar correspondence exists for wavelengths of at least a sixfold larger than the array aperture. Another interesting point is that the dispersion curves that we observe are sufficiently well constrained to show significant lateral changes in lithospheric structure within the French Alps over a distance of 50 km. Even though the interpretation of the dispersion curves is difficult, the obtained models are fully compatible with present models of the lithospheric structure in the area.

Another significant difficulty stems from the large uncertainties in the dispersion curves, which allow at best for retrieval of only major changes in mantle structure. An optimistic view would be that the French Alps are characterized by such strong heterogeneities that it is a particularly difficult study area, but further field experiments using similar array geometries in less extreme areas are required to validate this hypothesis. Another potential improvement would be an increase of the recording period, which would allow for an even more strict event selection. At present, field work is being carried out aimed at evaluating the array processing techniques, stretching from the relatively unperturbed areas west of the Alps to the very heterogeneous structure in the central Alps. If the conclusion of these studies is that array analysis is not adapted to lithospheric studies, it could nevertheless still provide a useful alternative to other array techniques at smaller scale, in particular in controlled source experiments in flat-layered geometries.

ACKNOWLEDGMENTS

The Briançon data were obtained as part of the GeoFrance-3D Alpes programme. The numerous people who participated in the field work are gratefully acknowledged, in particular J. Fréchet and R. Guiguet. We would also like to thank the people who hosted the seismic stations. Numerical simulations and inversions were carried out at the Centre de Calcul of the Observatoire de Grenoble. GMT software was used to create Fig. 7. We thank Günter Bock, Michael Korn and two anonymous reviewers for constructive comments.

REFERENCES

Arlitt, R., 1999. Teleseismic body wave tomography accross the Trans-European Suture Zone between Sweden and Denmark, *PhD thesis,* Institute of Geophysics, ETH Zurich.

Bear, L.K. & Pavlis, G.L., 1997. Estimation of slowness vectors and their uncertainties using multi-wavelet seismic array processing, *Bull. seism. Soc. Am.,* **87,** 755–769.

Bruneton, M., Farra, V. & Pedersen, H.A., 2002. Non-linear surface wave phase velocity inversion based on ray theory, *Geophys. J. Int.,* **151,** 583–596.

Capon, J., 1969. High-resolution frequency–wavenumber spectrum analysis, *Proc. IEEE,* **57,** 1408–1414.

Cattaneo, M., Augliera, P., Parolai, S. & Spalarossa, D., 1999. Anomalously deep earthquakes in northwestern Italy, *J. Seismol.,* **3,** 421–435.

Cotte, N., Pedersen, H.A., Campillo, M., Farra, V. & Cansi, Y., 2000. Off-great circle propagation of intermediate period surface waves observed on a dense array in the French Alps, *Geophys. J. Int.,* **142,** 825–840.

Cotte, N., Pedersen, H.A. & the TOR Working Group, 2002. Sharp contrast in lithospheric structure across the Sorgenfrei-Tornquist Zone as inferred by Rayleigh wave analysis of TOR1 project data, *Tectonophysics,* **360,** 75–88.

Dost, B., 1990. Upper mantle structure under Western Europe from fundamental and higher mode surface waves using the NARS array, *Geophys. J. Int.,* **100,** 131–151.

Frankel, A., Hough, S., Friberg, P. & Busby, R., 1991. Observations of Loma Prieta aftershocks from a dense array in Sunnyvale, California, *Bull. seism. Soc. Am.,* **5,** 1900–1922.

Friederich, W., 1998. Wave-theoretical inversion of teleseismic surface waves in a regional network: phase-velocity maps and a 3-D upper-mantle shear-wave velocity model for southern Germany, *Geophys. J. Int.,* **132,** 203–225.

Friederich, W. & Wielandt, E., 1995. Interpretation of seismic surface waves in regional networks: joint estimation of wavefield geometry and local phase velocity. Method and numerical tests, *Geophys. J. Int.,* **120,** 731–744.

Goldstein, P. & Archuleta, R., 1987. Array analysis of seismic signals, *Geophys. Res., Lett.,* **14,** 13–16.

Guyoton, F., 1991. Sismicité et structure lithsophérique des Alpes occidentales, *PhD thesis,* Université Joseph Fourier, Grenoble, France.

Herrin, E. & Goforth, T., 1977. Phase-matched filters: application to the study of Rayleigh waves, *Bull. seism. Soc. Am.,* **67,** 1259–1275.

Hwang, H.J. & Mitchell, B.J., 1986. Interstation surface wave analysis by frequency-domain Wiener deconvolution and modal isolation, *Bull. seism. Soc. Am.,* **76,** 847–864.

Levshin, A.L., Yanovskaia, T.B., Lander, A.V., Bukchin, B.G., Barmin, M.P., Ratnikova, L.I. & Its, E.N., 1989. Surface waves in vertically inhomogeneous media, in *Seismic Surface Waves in a Laterally Inhomogeneous Earth,* pp. 131–182, ed. Keilis-Borok, V.I., Kluwer, Dordrecht.

Mori, J., Filson, J., Cranswick, E., Borcherdt, R., Amirbekian, R., Aharonian, V. & Hachverdian, L., 1994. Measurements of *P* and *S* wave fronts from the dense three-dimensional array at Garni, Armenia, *Bull. seism. Soc. Am.,* **84,** 1089–1096.

Pedersen, H.A., S'anchez-Sesma, F.J. & Campillo, M., 1994. Three-dimensional scattering by two-dimensional topographies, *Bull. seism. Soc. Am.,* **94,** 1169–1183.

Pedersen, H.A., Maupin, V. & Campillo, M., 1996. Wave diffraction in multilayered media with the indirect boundary element method. Application to 3-D diffract ion of long period surface waves by 2-D lithospheric structures, *Geophys. J. Int.,* **125,** 545–558.

Pedersen, H.A., Avouac, J.-P. & Campillo, M., 1998. Anomalous surface waves from Lop Nor nuclear explosions: observations and numerical modelling, *J. geophys. Res.,* **103,** 15 051–15 068.

Plomerovà, J., Babuska, V., Vecsey, L., Kouba, D. & the TOR Working Group, 2002. Seismic anisotropy of the lithosphere around the Trans-European Suture Zone (TESZ) based on teleseismic body-wave data of the TOR experiment, *Tectonophysics,* **360,** 89–114.

Poupinet, G., Ellsworth, W. & Frechet, J., 1984. Monitoring velocity variations in the crust using earthquake doublets: an application to the Calaveras Fault, California, *J. geophys. Res.,* **89,** 5719–5731.

Sànchez-Sesma, F.J. & Campillo, M., 1993. Topographic effects for incident *P*, *SV*, and Rayleigh waves, *Tectonophysics,* **218,** 113–125.

Schmidt, R.O., 1986. Multiple emitter location and signal parameter estimation, *IEEE Trans. Antennas Propag.,* **34,** 276–280.

Shapiro, N.M., Campillo, M., Paul, A., Singh, S.K., Jongmans, D. & Sanchez-Sesma, F.J., 1997. Surface wave propagation across the Mexican Volcanic Belt and origin of the long-period seismic-wave amplification in the Valley of Mexico, *Geophys. J. Int.,* **128,** 151–166.

Shomali, Z.H., Roberts, R.G. & the TOR Working Group, 2002. Non-linear body wave teleseismic tomography along the TOR array, *Geophys. J. Int.,* **148,** 562–574.

Spakman, W., 1990. Tomographic images of the upper mantle below central Europe and the Mediterranean, *TerraNova,* **2,** 542–553.

Thouvenot, F., Paul, A., Fréchet, J., Béthoux, N., Jenatton, L. & Guiguet, R., 2002. 3-D constraints on the Moho in the south-western Alps: highlights of a new explosion–seismology experiment, submitted.

Yanovskaya, T.B., 1996. Ray tomography based on azimuthal anomalies, *Pure appl. Geophys.,* **148,** 319–336.

Wielandt, E., 1993. Propagation and structural interpretation of non-plane waves, *Geophys. J. Int.,* **113,** 45–53.

Wiener, N., 1949. *Time Series,* p. 163, MIT Press, Cambridge.